




**End-fire all-anisotropic transition metal dichalcogenide nanoantennas**Grigorios P. Zouros ,\* Georgios D. Kolezas , and George Fikioris *School of Electrical and Computer Engineering, National Technical University of Athens, 15773 Athens, Greece*Nikolaos L. Tsitsas *School of Informatics, Aristotle University of Thessaloniki, 54124 Thessaloniki, Greece*

(Received 29 August 2021; revised 7 December 2021; accepted 8 December 2021; published 23 December 2021)

We demonstrate that all-anisotropic transition metal dichalcogenide (TMDC) nanostructures can support advanced optical nanoantenna functionalities, such as high end-fire directivity and directionality inversion. The designed chain structures, driven by a dipole emitter, are composed of negative uniaxial anisotropic tungsten disulfide ( $\text{WS}_2$ ) TMDC nanoparticles featuring ordinary/extraordinary refractive indices. The ordinary index, whose values are much higher than those of Si (Si is typically used in all-dielectric nanostructures), is also much higher than the extraordinary index, thus allowing for a strong material birefringence. We find that anisotropy of this type makes it possible to achieve high end-fire directivity, and also offers an extra degree of freedom that allows for an orientation-based coupling between a free-to-rotate dipole emitter and fixed  $\text{WS}_2$  elements. Furthermore, appropriately rotating half the array elements achieves end-fire directional inversion (at a fixed operating wavelength) simply by adjusting the emitter orientation. This unique feature is characteristic of the high anisotropy exhibited by  $\text{WS}_2$  in the optical-near infrared regime, and cannot be readily realized with isotropic all-dielectric or plasmonic spherical structures due to their material symmetry. The presented material-anisotropy-based designs comprise a nanophotonics platform that allows for unique functionalities at the nanoscale, as well as for the implementation of tunable nanophotonic devices.

DOI: [10.1103/PhysRevB.104.245432](https://doi.org/10.1103/PhysRevB.104.245432)**I. INTRODUCTION**

In the last decade, nanophotonics has comprised a valuable platform for the development of functional optical devices due to the advancements in nanoscale fabrication of particles of various shapes and materials [1]. Such optical nanodevices have found a variety of applications, including enhanced light-matter interaction in all-dielectric structures [2,3], Purcell factor enhancement in plasmonic [4] or dielectric [5] nanocavities, Raman scattering from silicon nanodisks [6], plasmonic and all-dielectric optical directive nanoantennas [7–13], optical plasmonic spectrometers [14], fluorescence enhancement and control in plasmonic and silicon nanoparticles [15–17], and control of magnetic dipolar emission in plasmonics [18]. While the majority of the aforementioned applications is associated with all-dielectric and plasmonic structures, recently, another branch of anisotropic transition metal dichalcogenide (TMDC)-based nanophotonics [19–21] has emerged that aims to lead to unique effects and applications, such as exciton-polariton transport [22,23], tunable birefringence in Van Der Waals waveguides [24], and integration of TMDCs with dielectric nanostructures for the realization of integrated active metaoptical devices [25].

In this paper, we introduce all-anisotropic  $\text{WS}_2$  nanoantennas driven by dipole emitters and theoretically demonstrate that such structures can support high end-fire directivity and directionality inversion. To rigorously study this problem, we

develop a formal full-wave semianalytical solution for the radiation of an electric dipole source in the presence of an anisotropic spherical particle. The dipole can be located not only outside but also inside the anisotropic sphere. Although the application studied here exploits the part of the theory with the dipole outside, the remaining part can be potentially utilized in applications such as field-distribution modeling in deep brain stimulation [26] by considering spherical human head-dipole interactions [27], radiated power increments using double negative materials [28], fluorescence enhancement in metallic nanoshells [15], and Purcell factor studies [29]. The developed method includes, first, an extension of previous works [17,30,31] (that deal with the radiation problem of an infinitesimal electric dipole in the vicinity of an isotropic sphere) to the radiation problem of the same dipole in the vicinity of an anisotropic sphere, where the dipole can be placed inside or outside the anisotropic domain. Second, the calculation of the electric field is not based on the dyadic Green's function method [31,32], an approach feasible only when the medium surrounding the dipole is isotropic. Instead, to account for the anisotropy, we consider an equivalent surface current density produced by the dipole moment  $\mathbf{p}$  [33], express the electric field in subregions using appropriate expansions in spherical vector wave functions (SVWFs), and satisfy the necessary boundary conditions.

Initially, we consider a two-element  $\text{WS}_2$  sphere-dipole array, where one element is the  $\text{WS}_2$  nanoparticle and the other element is the emitter itself—usually a fluorescent molecule or a quantum dot—modeled as an infinitesimal electric Hertzian dipole, directed orthogonally with respect

\*zouros@ieee.org

to  $\text{WS}_2$ 's optic axis. Applying a multipolar decomposition for the total radiated field, we reveal that, when the dominant dipolar moments oscillate in phase, Huygens-like directivity—or radiation pattern—takes place, similar to the first Kerker condition of plane-wave scattering [34–36]. The fact that anisotropic particles support Huygens sources is based on experimental observations demonstrating that anisotropic TMDC nanostructures enter a regime of reduced backscattering that corresponds to the first Kerker condition characterized by a large forward-to-backward scattering ratio [20]; yet, this first Kerker condition stems from the Huygens source [34]. To fully understand this particular behavior, we also perform electromagnetic (EM) plane-wave scattering calculations using a rigorous semianalytical solution [35] and show that individual  $\text{WS}_2$  nanoparticles can support magnetic dipolar (MD) and electric dipolar (ED) resonances in the visible regime, similar to high-index isotropic dielectrics. This allows us to explain that Huygens-like directivity occurs when the radiation wavelength of the dipole is in the vicinity of the  $\text{WS}_2$  particle's ED resonance. On the contrary, when the dipole is parallel to  $\text{WS}_2$ 's optic axis, no specific constructive or destructive behavior in the oscillating MD/ED moments is observed and therefore Huygens-like directivity is not supported. This is a consequence of the high anisotropy ratio (AR) exhibited by  $\text{WS}_2$ . Based on these principles, we further demonstrate via full-wave finite-element simulations (using the high-frequency structure simulator—HFSS) that chain structures of spherical or cylindrical disk  $\text{WS}_2$  elements may serve as high end-fire directivity nanoantenna arrays which actually enhance the directivity of the two-element counterpart that supports Huygens-like source. The size of each individual element is appropriately selected so its ED resonance is shifted in a desired operating wavelength regime.

We further reveal that material anisotropy strongly affects the response of a nanoantenna array with respect to the orientation of the emitter, thus allowing for an extra degree of freedom in the design of radiating nanostructures. In particular, it is possible to utilize the material anisotropy to achieve directionality inversion for the same operating wavelength with an exactly symmetric radiation pattern in the two directions—forward and backward—along the axis of the nanoantenna. This feature is characteristic of the material anisotropy and can be achieved in chains of single  $\text{WS}_2$  particles, but not with simple isotropic dielectric spherical structures due to the material symmetry of the latter; achieving an equivalent behavior requires more complex configurations, like chains of isotropic core-shell nanoparticles with proper external pumping [13] or chains of magnetodielectric particles with Huygens source excitation, i.e., a source composed of mutually orthogonal electric and magnetic dipoles [37]. Another major advantage of our design is that precise directionality inversion (due to material anisotropy) takes place at a fixed operating wavelength, in contrast to core-shell isotropic plasmonic configurations where inversion is obtained at different wavelengths [14]. All in all, the role of anisotropy is to render the operation of the two-element  $\text{WS}_2$  sphere-dipole array, as well as of the chain of spherical  $\text{WS}_2$  elements, dependent on the relative orientation of the dipole emitter, and to allow for directionality inversion.

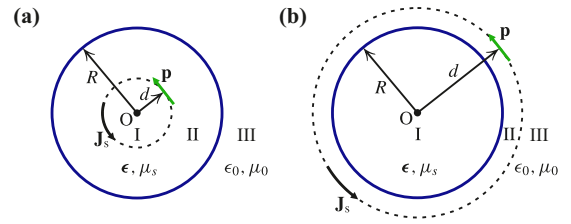


FIG. 1. (a) Dipole inside the anisotropic sphere. (b) Dipole outside the anisotropic sphere.

The remainder of the paper is organized as follows. In Sec. II, we develop the full-wave semianalytical solution for the radiation problem of an electric dipole source in the presence of an anisotropic spherical particle and in Sec. III we analyze the two-element TMDC sphere-dipole array based on the developed method. In Secs. IV and V, we discuss properties such as high end-fire directivity and directionality inversion, and Sec. VI concludes the paper.

## II. FULL-WAVE SEMIANALYTICAL SOLUTION

In this section, we develop a full-wave semianalytical solution for the radiation of an electric dipole source in the presence of an anisotropic spherical particle. The dipole can be located outside or inside the anisotropic sphere. The two radiation problems (dipole inside and outside the anisotropic sphere) are depicted in Fig. 1. The sphere has radius  $R$  and its EM properties are described by the Cartesian anisotropic permittivity tensor,

$$\bar{\bar{\epsilon}} = \begin{bmatrix} \epsilon_1 & 0 & 0 \\ 0 & \epsilon_1 & 0 \\ 0 & 0 & \epsilon_3 \end{bmatrix}, \quad (1)$$

and the scalar permeability  $\mu_s$ . The medium surrounding the sphere is free space with permittivity  $\epsilon_0$  and permeability  $\mu_0$ . Assuming a spherical coordinate system whose origin is at the center of the sphere, we consider a tangential point electric dipole with dipole moment  $\mathbf{p} = p_\theta \mathbf{e}_\theta + p_\varphi \mathbf{e}_\varphi$ , located at  $\mathbf{r}_d = (d, \theta_d, \varphi_d)$ . The time dependence  $e^{-i\omega t}$  is assumed and suppressed throughout.

### A. Dipole inside the sphere

We begin by examining the case where the dipole source is located inside the anisotropic sphere—i.e.,  $d < R$ —as depicted in Fig. 1(a). The presence of the dipole at  $\mathbf{r}_d$  introduces a discontinuity at the spherical surface  $r = d$ . As a consequence, our analysis is carried out by separating the interior of the sphere into two regions, namely, region I with  $0 \leq r < d$  and region II with  $d < r < R$ . Both regions are anisotropic with the same EM properties. Therefore, the electric field in each respective region can be expressed in terms of SVWFs by employing the expansions [38]

$$\mathbf{E}^I = \sum_{n=1}^{\infty} \sum_{m=-n}^n \bar{E}_{mn} \sum_{l=1}^{\infty} \alpha_l \left[ c_{mnl} \mathbf{M}_{mn}^{(1)}(k_l, \mathbf{r}) + d_{mnl} \mathbf{N}_{mn}^{(1)}(k_l, \mathbf{r}) + \frac{\bar{w}_{mnl}}{\lambda_l} \mathbf{L}_{mn}^{(1)}(k_l, \mathbf{r}) \right] + \sum_{l=1}^{\infty} \alpha_l \frac{w_{00l}}{\lambda_l} \mathbf{L}_{00}^{(1)}(k_l, \mathbf{r}), \quad (2)$$

$$\begin{aligned} \mathbf{E}^{\text{II}} = & \sum_{n=1}^{\infty} \sum_{m=-n}^n \bar{E}_{mn} \sum_{l=1}^{\infty} \sum_{j=1,3} \beta_l^{(j)} \left[ c_{mnl} \mathbf{M}_{mn}^{(j)}(k_l, \mathbf{r}) \right. \\ & \left. + d_{mnl} \mathbf{N}_{mn}^{(j)}(k_l, \mathbf{r}) + \frac{\bar{w}_{mnl}}{\lambda_l} \mathbf{L}_{mn}^{(j)}(k_l, \mathbf{r}) \right] \\ & + \sum_{l=1}^{\infty} \sum_{j=1,3} \beta_l^{(j)} \frac{w_{00l}}{\lambda_l} \mathbf{L}_{00}^{(j)}(k_l, \mathbf{r}). \end{aligned} \quad (3)$$

In Eqs. (2) and (3),  $\mathbf{M}_{mn}^{(j)}$ ,  $\mathbf{N}_{mn}^{(j)}$ , and  $\mathbf{L}_{mn}^{(j)}$  are the SVWFs of the first ( $j = 1$ ) and third ( $j = 3$ ) kind [39], while  $\bar{E}_{mn} = i^n \{(2n+1)(n-m)!/[n(n+1)(n+m)!]\}^{1/2}$ . In addition,  $\alpha_l$ ,  $\beta_l^{(1)}$ , and  $\beta_l^{(3)}$  are unknown expansion coefficients, whereas  $c_{mnl}$ ,  $d_{mnl}$ ,  $\bar{w}_{mnl}$ ,  $w_{00l}$ , and  $\lambda_l$  are known quantities, obtained by solving an eigenvalue problem whose matrix depends on the elements of the permittivity tensor [38]. Finally, the discrete wave number  $k_l$  is given by  $k_l = \omega(\epsilon_3 \mu_s / \lambda_l)^{1/2}$  [38]. We note that  $c_{mnl}$ ,  $d_{mnl}$ ,  $\bar{w}_{mnl}$ ,  $w_{00l}$ ,  $\lambda_l$ , and  $k_l$  in the field expansions of Eqs. (2) and (3) are the same, since regions I and II have the same EM properties.

The radiated electric field in region III external to the sphere—i.e., for  $r > d$ —may also be expressed as an expansion of SVWFs, in the form

$$\mathbf{E}^{\text{rad}} = \sum_{n=1}^{\infty} \sum_{m=-n}^n \bar{E}_{mn} [a_{mn} \mathbf{M}_{mn}^{(3)}(k_0, \mathbf{r}) + b_{mn} \mathbf{N}_{mn}^{(3)}(k_0, \mathbf{r})], \quad (4)$$

where  $k_0 = \omega(\epsilon_0 \mu_0)^{1/2}$  and  $a_{mn}$  and  $b_{mn}$  are unknown expansion coefficients. The expansions of the corresponding magnetic fields  $\mathbf{H}^{\text{I}}$ ,  $\mathbf{H}^{\text{II}}$ , and  $\mathbf{H}^{\text{rad}}$  are obtained from the Maxwell-Faraday equation  $\mathbf{H} = -i/(\omega\mu)\nabla \times \mathbf{E}$ .

Next we proceed to impose the boundary conditions for the tangential components of the electric and the magnetic fields on the surfaces  $r = d$  and  $r = R$ . To this end, the dipole source at  $\mathbf{r}_d$  is taken into account by considering an equivalent surface current density given by [33]

$$\mathbf{J}_s = \frac{\delta(\theta - \theta_d) \delta(\varphi - \varphi_d)}{d^2 \sin \theta} \mathbf{p}, \quad (5)$$

and the boundary conditions that must be satisfied are  $\mathbf{e}_r \times (\mathbf{E}^{\text{II}} - \mathbf{E}^{\text{I}})|_{r=d} = \mathbf{0}$ ,  $\mathbf{e}_r \times (\mathbf{H}^{\text{II}} - \mathbf{H}^{\text{I}})|_{r=d} = \mathbf{J}_s$  and  $\mathbf{e}_r \times (\mathbf{E}^{\text{rad}} - \mathbf{E}^{\text{II}})|_{r=R} = \mathbf{0}$ ,  $\mathbf{e}_r \times (\mathbf{H}^{\text{rad}} - \mathbf{H}^{\text{II}})|_{r=R} = \mathbf{0}$ . Substituting the field expansions into the two boundary conditions for  $r = d$  and making use of the orthogonality properties of the spherical vector harmonics [40], we finally arrive at the following system of linear equations for the unknown expansion coefficients:

$$\sum_{l=1}^{\infty} c_{mnl} [\beta_l^{(1)} j_n(y_l) + \beta_l^{(3)} h_n(y_l) - \alpha_l j_n(y_l)] = 0, \quad (6)$$

$$\begin{aligned} & \sum_{l=1}^{\infty} \frac{1}{y_l} \left\{ d_{mnl} [\beta_l^{(1)} j_n^d(y_l) + \beta_l^{(3)} h_n^d(y_l) - \alpha_l j_n^d(y_l)] \right. \\ & \left. + \frac{\bar{w}_{mnl}}{\lambda_l} [\beta_l^{(1)} j_n(y_l) + \beta_l^{(3)} h_n(y_l) - \alpha_l j_n(y_l)] \right\} = 0, \end{aligned} \quad (7)$$

$$\begin{aligned} & \sum_{l=1}^{\infty} y_l d_{mnl} [\beta_l^{(1)} j_n(y_l) + \beta_l^{(3)} h_n(y_l) - \alpha_l j_n(y_l)] \\ & = \frac{i^{-2n+1} \omega \mu_s}{4\pi d} \bar{E}_{mn} \sqrt{n(n+1)} \mathbf{p} \cdot \mathbf{B}_{mn}^*(\theta_d, \varphi_d), \end{aligned} \quad (8)$$

$$\begin{aligned} & \sum_{l=1}^{\infty} c_{mnl} [\beta_l^{(1)} j_n^d(y_l) + \beta_l^{(3)} h_n^d(y_l) - \alpha_l j_n^d(y_l)] \\ & = - \frac{i^{-2n+1} \omega \mu_s}{4\pi d} \bar{E}_{mn} \sqrt{n(n+1)} \mathbf{p} \cdot \mathbf{C}_{mn}^*(\theta_d, \varphi_d), \end{aligned} \quad (9)$$

where  $j_n$  is the spherical Bessel function,  $h_n$  is the spherical Hankel function of the first kind,  $z_n^d(x) \equiv z_n(x) + x z_n'(x)$  (with  $z_n = j_n, h_n$  and the prime denoting derivative with respect to the argument),  $y_l = k_l d$ ,  $\mathbf{B}_{mn}$  and  $\mathbf{C}_{mn}$  the spherical vector harmonics [40], and the asterisk denotes complex conjugation. In a similar manner, the two boundary conditions for  $r = R$  yield the following equations:

$$\sum_{l=1}^{\infty} c_{mnl} [\beta_l^{(1)} j_n(x_l) + \beta_l^{(3)} h_n(x_l)] - a_{mn} h_n(x_0) = 0, \quad (10)$$

$$\begin{aligned} & \sum_{l=1}^{\infty} \frac{x_0}{x_l} \left\{ d_{mnl} [\beta_l^{(1)} j_n^d(x_l) + \beta_l^{(3)} h_n^d(x_l)] \right. \\ & \left. + \frac{\bar{w}_{mnl}}{\lambda_l} [\beta_l^{(1)} j_n(x_l) + \beta_l^{(3)} h_n(x_l)] \right\} - b_{mn} h_n^d(x_0) = 0, \end{aligned} \quad (11)$$

$$\sum_{l=1}^{\infty} \frac{x_l}{x_0} d_{mnl} [\beta_l^{(1)} j_n(x_l) + \beta_l^{(3)} h_n(x_l)] - b_{mn} \mu_{sr} h_n(x_0) = 0, \quad (12)$$

$$\sum_{l=1}^{\infty} c_{mnl} [\beta_l^{(1)} j_n^d(x_l) + \beta_l^{(3)} h_n^d(x_l)] - a_{mn} \mu_{sr} h_n^d(x_0) = 0, \quad (13)$$

where  $x_l = k_l R$ ,  $x_0 = k_0 R$ , and  $\mu_{sr} = \mu_s / \mu_0$ . Equations (6)–(13) comprise an infinite linear system that—upon truncation—can be solved for the coefficients  $a_{mn}$  and  $b_{mn}$  of the field.

## B. Dipole outside the sphere

The case of the dipole source located outside the anisotropic sphere—i.e.,  $d > R$ —is treated in a manner similar to the one presented in the previous subsection. The configuration of this problem is depicted in Fig. 1(b). In particular, owing to the presence of the dipole at  $\mathbf{r}_d$ , the exterior of the sphere is separated into two regions, namely, region II with  $R < r < d$  and region III with  $r > d$ . The electric field in region II can be written as

$$\begin{aligned} \mathbf{E}^{\text{II}} = & \sum_{n=1}^{\infty} \sum_{m=-n}^n \bar{E}_{mn} [c_{mn} \mathbf{M}_{mn}^{(1)}(k_0, \mathbf{r}) + d_{mn} \mathbf{N}_{mn}^{(1)}(k_0, \mathbf{r}) \\ & + f_{mn} \mathbf{M}_{mn}^{(3)}(k_0, \mathbf{r}) + g_{mn} \mathbf{N}_{mn}^{(3)}(k_0, \mathbf{r})], \end{aligned} \quad (14)$$

with  $c_{mn}$ ,  $d_{mn}$ ,  $f_{mn}$ , and  $g_{mn}$  unknown expansion coefficients, while in region III  $\mathbf{E}^{\text{rad}}$  has the same expression as with Eq. (4). The electric field at the interior of the sphere (region I) has the same expression as Eq. (2). Again, the corresponding magnetic fields are found by the Maxwell-Faraday equation.

The boundary conditions that must now hold are  $\mathbf{e}_r \times (\mathbf{E}^{\text{II}} - \mathbf{E}^{\text{I}})|_{r=R} = \mathbf{0}$ ,  $\mathbf{e}_r \times (\mathbf{H}^{\text{II}} - \mathbf{H}^{\text{I}})|_{r=R} = \mathbf{0}$  and  $\mathbf{e}_r \times (\mathbf{E}^{\text{rad}} - \mathbf{E}^{\text{II}})|_{r=d} = \mathbf{0}$ ,  $\mathbf{e}_r \times (\mathbf{H}^{\text{rad}} - \mathbf{H}^{\text{II}})|_{r=d} = \mathbf{J}_s$ . Following

the same steps as in Sec. II A, the two boundary conditions for  $r = R$  yield the equations

$$c_{mn}j_n(x_0) + f_{mn}h_n(x_0) - \sum_{l=1}^{\infty} \alpha_l c_{mnl} j_n(x_l) = 0, \quad (15)$$

$$d_{mn}j_n^d(x_0) + g_{mn}h_n^d(x_0) - \sum_{l=1}^{\infty} \alpha_l \frac{x_0}{x_l} \left[ d_{mnl} j_n^d(x_l) + \frac{\bar{w}_{mnl}}{\lambda_l} j_n(x_l) \right] = 0, \quad (16)$$

$$d_{mn}\mu_{sr}j_n(x_0) + g_{mn}\mu_{sr}h_n(x_0) - \sum_{l=1}^{\infty} \alpha_l \frac{x_l}{x_0} d_{mnl} j_n(x_l) = 0, \quad (17)$$

$$c_{mn}\mu_{sr}j_n^d(x_0) + f_{mn}\mu_{sr}h_n^d(x_0) - \sum_{l=1}^{\infty} \alpha_l c_{mnl} j_n^d(x_l) = 0, \quad (18)$$

and the two boundary conditions for  $r = d$ , the equations

$$a_{mn}h_n(x_d) - c_{mn}j_n(x_d) - f_{mn}h_n(x_d) = 0, \quad (19)$$

$$b_{mn}h_n^d(x_d) - d_{mn}j_n^d(x_d) - g_{mn}h_n^d(x_d) = 0, \quad (20)$$

$$b_{mn}h_n(x_d) - d_{mn}j_n(x_d) - g_{mn}h_n(x_d) = \frac{i^{-2n+1}\omega\mu_0}{4\pi dx_d} \bar{E}_{mn} \sqrt{n(n+1)} \mathbf{p} \cdot \mathbf{B}_{mn}^*(\theta_d, \varphi_d), \quad (21)$$

$$a_{mn}h_n^d(x_d) - c_{mn}j_n^d(x_d) - f_{mn}h_n^d(x_d) = -\frac{i^{-2n+1}\omega\mu_0}{4\pi d} \bar{E}_{mn} \sqrt{n(n+1)} \mathbf{p} \cdot \mathbf{C}_{mn}^*(\theta_d, \varphi_d), \quad (22)$$

where  $x_d = k_0 d$ . As in the previous subsection, Eqs. (15)–(22) comprise an infinite linear system that—upon truncation—can be solved for the coefficients  $a_{mn}$  and  $b_{mn}$  of the radiated field.

### C. Far field and directivity

Employing the large argument asymptotic expansions for the Hankel function of the first kind and its derivative, it is straightforward to express the total radiated electric far field as

$$\mathbf{E}^{\text{rad}} \underset{k_0 r \gg 1}{\sim} \frac{e^{ik_0 r}}{r} \mathbf{f}(\theta, \varphi), \quad (23)$$

where  $\mathbf{f}(\theta, \varphi) = f_\theta(\theta, \varphi)\mathbf{e}_\theta + f_\varphi(\theta, \varphi)\mathbf{e}_\varphi$  is the scattering amplitude and

$$f_\theta(\theta, \varphi) = \frac{1}{k_0} \sum_{n=1}^{\infty} \sum_{m=-n}^n i^{-n} \bar{E}_{mn} \left[ \frac{m}{\sin \theta} P_n^m(\cos \theta) a_{mn} + \frac{dP_n^m(\cos \theta)}{d\theta} b_{mn} \right] e^{im\varphi}, \quad (24)$$

$$f_\varphi(\theta, \varphi) = \frac{1}{k_0} \sum_{n=1}^{\infty} \sum_{m=-n}^n i^{-n+1} \bar{E}_{mn} \left[ \frac{dP_n^m(\cos \theta)}{d\theta} a_{mn} + \frac{m}{\sin \theta} P_n^m(\cos \theta) b_{mn} \right] e^{im\varphi}, \quad (25)$$

where  $P_n^m$  the associated Legendre functions. The total radiated magnetic far-field is given by  $\mathbf{H}^{\text{rad}} = -i/(\omega\mu_0)\nabla \times \mathbf{E}^{\text{rad}}$ .

The radiation pattern—i.e., the far-field response—of an antenna is described by the directivity defined by [41]

$$D(\theta, \varphi) = \frac{4\pi U(\theta, \varphi)}{P_{\text{rad}}}, \quad (26)$$

where  $U = r^2 \mathbf{S}^{\text{rad}} \cdot \mathbf{e}_r$  is the radiation intensity—with  $\mathbf{S}^{\text{rad}}$  the time-averaged radiated power flow—and  $P_{\text{rad}}$  the total radiated power in the far-field. Using the relations  $\mathbf{S}^{\text{rad}} = 1/2 \text{Re}\{\mathbf{E}^{\text{rad}} \times (\mathbf{H}^{\text{rad}})^*\}$ —where  $\text{Re}$  denotes the real part—and  $P_{\text{rad}} = \oint \mathbf{S}^{\text{rad}} \cdot \mathbf{e}_r dS$ —where  $dS$  is the differential surface of a  $r$ -radius sphere—Eq. (26) can be written in the form

$$D(\theta, \varphi) = \frac{4\pi^2}{\lambda_0^2} \frac{|f_\theta(\theta, \varphi)|^2 + |f_\varphi(\theta, \varphi)|^2}{\sum_{n=1}^{\infty} \sum_{m=-n}^n (|a_{mn}|^2 + |b_{mn}|^2)}, \quad (27)$$

with  $\lambda_0$  the radiation wavelength.

Depending on the position and orientation of the dipole, Eqs. (6)–(13) or Eqs. (15)–(22) can be solved for the expansion coefficients  $a_{mn}$  and  $b_{mn}$ . Then, with the aid of Eqs. (24), (25), and (27),  $D(\theta, \varphi)$  can be readily computed.

### III. TWO-ELEMENT TMDC SPHERE-DIPOLE ARRAY

The proposed nanoantenna designs are based on  $\text{WS}_2$ , a nonmagnetic ( $\mu_s = \mu_0$ ) multilayer TMDC material described by a dispersive negative uniaxial (NU) anisotropic permittivity tensor [19] given by Eq. (1) as  $\bar{\epsilon}(\lambda_0) = \epsilon_1(\lambda_0)(\mathbf{e}_x \mathbf{e}_x^T + \mathbf{e}_y \mathbf{e}_y^T) + \epsilon_3(\lambda_0) \mathbf{e}_z \mathbf{e}_z^T$ , where  $T$  denotes transposition. In this tensorial form,  $\epsilon_1$  and  $\epsilon_3$  are the ordinary and extraordinary elements, respectively—also called in-plane/out-of-plane dielectric functions—and the optic axis of the material coincides with the  $z$  axis. Throughout this paper, we employ realistic dispersive properties for  $\epsilon_1$  and  $\epsilon_3$  in the visible-near infrared (IR) regime of 500 nm–1200 nm, as shown in Fig. 1(a) of Ref. [19]. For wavelengths from 500 nm up to 826.6 nm—where 826.6 nm is the upper dispersion limit for Si [42]— $\text{Re}\{\epsilon_1\} > \text{Re}\{\epsilon_3\}$ , with the latter being the real part of Si permittivity (Si is the most usual material for all-dielectric nanostructures). These large ordinary permittivity values support MD/ED resonances similar to high-index isotropic dielectrics. In addition,  $\text{Re}\{\epsilon_3\}$  is significantly lower than  $\text{Re}\{\epsilon_1\}$  in the whole 500 nm–1200 nm range—thus  $\text{WS}_2$  is NU—resulting in a high AR useful in the implementation of a functional directionality inversion.

As a first step toward the implementation of larger nanoantenna arrays, we consider a two-element sphere-dipole array consisting of a  $\text{WS}_2$  nanosphere with radius  $R = 100$  nm and a horizontal ( $y$ -oriented) infinitesimal electric Hertzian dipole whose moment is directed along the  $+y$  axis and is located at  $x = d = 200$  nm, i.e., 100 nm from the sphere's surface, as illustrated in the inset of Fig. 2(a). The optic axis of the  $\text{WS}_2$  sphere coincides with the  $z$  axis. To rigorously study this two-element array, we employ the full-wave semianalytical solution developed in Sec. II. The far-field response of the sphere-dipole array is described by its directivity  $D(\theta, \varphi)$  via Eq. (27). In Fig. 2(a), we plot  $D_0 \equiv D(90^\circ, 0^\circ)$  and  $D_{180} \equiv D(90^\circ, 180^\circ)$ , as observed at  $+x$  and  $-x$  axis, respectively, as a function of  $\lambda_0$ . The criterion for truncating the infinite matrix equation—i.e., the matrix constructed by Eqs. (15)–(22)—is to establish six accurate significant figures in the value of directivity  $D(\theta, \varphi)$ . To achieve this goal, an upper truncation

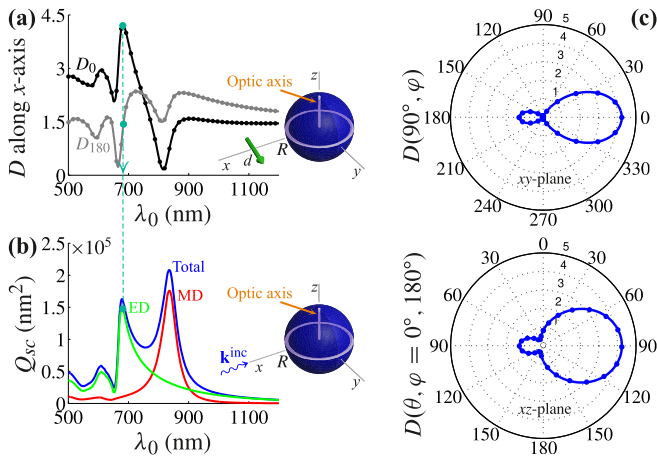


FIG. 2. (a) Directivities along the  $x$  axis of the 100-nm-radius  $\text{WS}_2$  sphere-dipole array, with the dipole located at 200 nm on  $x$  axis. Black:  $D_0 \equiv D(90^\circ, 0^\circ)$  at  $+x$  axis; black curve: semianalytical method; black dots: HFSS. Gray:  $D_{180} \equiv D(90^\circ, 180^\circ)$  at  $-x$  axis; gray curve: semianalytical method; gray dots: HFSS. Green dashed arrowhead line:  $\lambda_0 = 681$  nm [close vicinity of ED resonance—see Fig. 2(b)]. Inset: Radiation problem of a  $\text{WS}_2$  sphere excited by a  $y$ -oriented electric dipole. The optic axis of the sphere coincides with the  $z$  axis. (b) Plane-wave scattering spectrum of a 100-nm-radius  $\text{WS}_2$  sphere illuminated by a TE polarized plane wave impinging from the  $+x$  axis (via Ref. [35]). Blue: Total  $Q_{sc}$ ; red: MD term; green: ED term. Green dashed line: Projection of 681 nm (the ED resonance is located at 679 nm and the MD resonance at 836 nm). Inset: Plane-wave scattering from a  $\text{WS}_2$  sphere. (c) Directivities on  $xy$  and  $xz$  planes when the dipole radiates at 681 nm. Blue curves: Semianalytical method; blue dots: HFSS.

bound of  $N_c = 8$  is used in the  $n$ -index series for the computation of  $D(\theta, \varphi)$  from Eq. (27) [we note that the truncation bound  $L_c$  in the  $l$ -index series in Eqs. (15)–(18) follows the rule  $L_c = 2N_c$ ]. The black/gray curves are computed with this  $N_c$  value by our semianalytical method and are in excellent agreement with the HFSS's finite-element solver (black/gray dots). The  $\max\{D_0\} = 4.23$  in the visible-near IR dispersive range of  $\text{WS}_2$  is observed at  $\lambda_0 = 681$  nm; at this  $\lambda_0$ , it is seen that  $D_{180} = 1.29$ . To better understand the spectral response of the  $\text{WS}_2$  nanosphere in the array, we calculate the EM scattering from this same 100 nm-radius sphere of a transverse electric (TE) plane wave, i.e.,  $\mathbf{E}^{\text{inc}}$  is  $y$  polarized and  $\mathbf{k}^{\text{inc}}$  is directed along the  $+x$  axis, as depicted in the inset of Fig. 2(b). The polarization and angle of incidence considered in the plane wave are consistent with the dipole excitation used in Fig. 2(a), i.e., the ED response produced in the far-field of both problems is characterized by the same spherical harmonics indices. In the plane-wave incidence case, employing a rigorous semianalytical solution for the EM scattering from anisotropic particles [35], we find that the scattering cross section is given by (see the first of Eq. (15) in Ref. [35])

$$Q_{sc} = \frac{\lambda_0^2}{\pi} \sum_{n=1}^{\infty} \sum_{m=-n}^n (|A_{mn}|^2 + |B_{mn}|^2). \quad (28)$$

In Eq. (28),  $A_{mn}$  and  $B_{mn}$  are the expansion coefficients of the scattered electric field, when the latter is expanded in SVWFs

as given by Eq. (4) of Ref. [35]—in Ref. [35],  $A_{mn}$  and  $B_{mn}$  are represented, respectively, by  $a_{mn}^{(0)}$  and  $b_{mn}^{(0)}$ . It should be clarified that the expansion coefficients  $A_{mn}$  and  $B_{mn}$  in Eq. (28) are not the same with  $a_{mn}$  and  $b_{mn}$  in Eqs. (24) and (25). The former are obtained from the solution of EM plane-wave scattering and are computed, after truncation, from the four infinite sets of equations given by Eq. (12) in Ref. [35]. On the contrary,  $a_{mn}$  and  $b_{mn}$  are the expansion coefficients of the radiated electric field given by Eq. (4), obtained from the solution of the radiation problem of an electric dipole in the presence of an anisotropic sphere and computed, after truncation, from the eight infinite sets of equations given by Eqs. (6)–(13) or Eqs. (15)–(22). In the long-wavelength limit, the spectrum is dominated by MD and ED responses for which  $n = 1$ ; the MD response is obtained from Eq. (28) when  $Q_{sc}$  is determined exclusively from  $A_{m1}$  and the ED response solely from  $B_{m1}$ , with  $m = 0$  or  $\pm 1$ , depending on the angle of incidence. In the configuration of Fig. 2(b), the nonzero expansion coefficients are  $A_{01}$  and  $B_{\pm 1,1}$ . Figure 2(b) reveals that a  $\text{WS}_2$  nanosphere can support a MD resonance at 836 nm and an ED resonance at 679 nm, similarly to the subwavelength spectrum of high-index dielectrics [34]. The radiation and scattering responses of Figs. 2(a) and 2(b) show that  $\max\{D_0\}$  takes place when the dipole radiates in the vicinity of the sphere's ED resonance. Consequently, at the spectral location of optimized radiation—i.e., at maximum  $D_0$ —the nanosphere can be considered as an electric dipole element that combines with the dipole emitter to form a nanoantenna dipole array. Figure 2(c) depicts  $D$  on the  $xy$  (top) and  $xz$  planes (bottom), when the sphere-dipole array radiates exactly at 681 nm, i.e., the location of  $\max\{D_0\}$ . The validity of our computations is established, since our semianalytical method (blue curves) is in excellent agreement with HFSS (blue dots). This operation results in a Huygens-like directivity [43], i.e., significant radiation in one direction—in this case toward the  $+x$  axis—and suppressed radiation in the opposite.

To fully elucidate the physical mechanism of this Huygens-like radiation, we employ the decomposition  $\mathbf{E}^{\text{rad}} = \mathbf{E}_s^{\text{rad}} + \mathbf{E}_d^{\text{rad}}$  for the total electric field  $\mathbf{E}^{\text{rad}}$  radiated from the sphere-dipole system, where  $\mathbf{E}_s^{\text{rad}}$  is the field radiated—i.e., scattered—from the sphere, and  $\mathbf{E}_d^{\text{rad}}$  is the field radiated from the dipole. We then consider the multipolar decomposition of each of the above-mentioned radiated fields, i.e., we first express  $\mathbf{E}_s^{\text{rad}}$  and  $\mathbf{E}_d^{\text{rad}}$  in a form similar to  $\mathbf{E}^{\text{rad}}$ —see Eq. (4)—and then we calculate the respective expansion coefficients ( $a_{mn}^s$ ,  $b_{mn}^s$  for  $\mathbf{E}_s^{\text{rad}}$  and  $a_{mn}^d$ ,  $b_{mn}^d$  for  $\mathbf{E}_d^{\text{rad}}$ ). The expansion coefficients' magnitudes of the sphere, dipole, and sphere-dipole setups are plotted in Figs. 3(a)–3(c), respectively (in each subfigure, we also depict the respective setup). The normalized magnitudes of the dominant expansion coefficients in Fig. 3(a) are plotted in the spectral window of 500 nm–1200 nm. In this regime, the contribution of  $\mathbf{E}_s^{\text{rad}}$  stems from  $a_{01}^s$  (MD moment),  $b_{\pm 1,1}^s$  (ED moment),  $a_{\pm 1,2}^s$  [magnetic quadrupolar (MQ) moment], and  $b_{\pm 2,2}^s$  [electric quadrupolar (EQ) moment]. The magnitudes of the remaining MD/ED/MQ/EQ moments—i.e.,  $a_{\pm 1,1}^s$ ,  $b_{01}^s$ ,  $a_{02}^s$ ,  $a_{\pm 2,2}^s$ ,  $b_{02}^s$ , and  $b_{\pm 1,2}^s$ —as well as those of higher order moments, are negligible in this regime. In all Figs. 3(a)–3(c), the magnitudes are plotted normalized—indicated by the subscript  $N$ —with respect to the maximum magnitude in this spectral window. It should be noted that the expansion

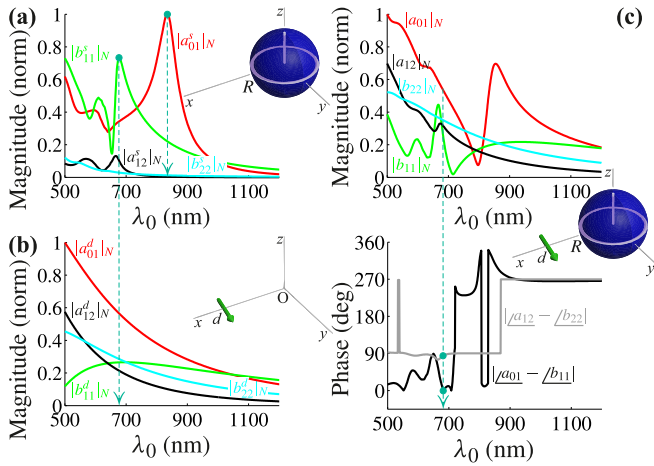


FIG. 3. Multipolar decomposition for the independent elements of the sphere-dipole array of Fig. 2(a)/inset and for the array as a whole. (a) Normalized magnitudes of the dominant electric and magnetic expansion coefficients from the sole contribution of the sphere. Red:  $|a_{01}^s|_N$  (MD moment); green:  $|b_{11}^s|_N$  (ED moment); black:  $|a_{12}^s|_N$  (MQ moment); cyan:  $|b_{22}^s|_N$  (EQ moment). The left green dashed line indicates the position of  $\max\{|b_{11}^s|_N\}$  at 679 nm; the right green dashed line indicates the position of  $\max\{|a_{01}^s|_N\}$  at 836 nm. (b) Normalized magnitudes of the dominant electric and magnetic expansion coefficients from the sole contribution of the dipole. Red:  $|a_{01}^d|_N$  (MD moment); green:  $|b_{11}^d|_N$  (ED moment); black:  $|a_{12}^d|_N$  (MQ moment); cyan:  $|b_{22}^d|_N$  (EQ moment). (c) Top: Normalized magnitudes of the dominant electric and magnetic expansion coefficients from the sphere-dipole array. Red:  $|a_{01}|_N$  (MD moment); green:  $|b_{11}|_N$  (ED moment); black:  $|a_{12}|_N$  (MQ moment); cyan:  $|b_{22}|_N$  (EQ moment). Bottom: absolute phase difference between MD/ED and MQ/EQ moments. Black:  $|a_{01} - b_{11}|$ ; gray:  $|a_{12} - b_{22}|$ . Green dashed arrowhead line:  $\lambda_0 = 681$  nm where Huygens-like directivity is achieved [see Figs. 2(a) and 2(c)].

coefficients with spherical harmonics indices  $\pm|m|$  have the same magnitude, so only  $+|m|$  is shown. This last remark holds for Figs. 3(b) and 3(c) as well. With respect to Fig. 3(a), at 679 nm—indicated by a green dashed line—it is the ED moment that exhibits its maximum and is dominant with respect to other moments. This position corresponds to the ED resonance of the sphere [see Fig. 2(b)]. On the other hand, at 836 nm—also indicated by a green dashed line—the MD moment exhibits its maximum and is dominant with respect to other moments, and this position corresponds to the MD resonance of the sphere [see Fig. 2(b)]. However, this wavelength does not pertain to the optimal radiation of the sphere-dipole array, which occurs in the vicinity of the ED resonance [see Fig. 2(a)]. Figure 3(b) shows that the contribution in  $\mathbf{E}_d^{\text{rad}}$  stems from the same dipolar and quadrupolar moments as with the ones for  $\mathbf{E}_s^{\text{rad}}$ . The electric dipole itself exhibits MD and MQ/EQ moments (and not only the ED moment) because it is placed eccentrically at  $x = d = 200$  nm. If the dipole is placed at the origin, the contribution in  $\mathbf{E}_d^{\text{rad}}$  stems exclusively from the ED moment  $b_{\pm 1,1}^d$ . The insights gained by Figs. 3(a) and 3(b) further establish the above-mentioned observation that, at the spectral location of optimized radiation—i.e., at  $\max\{D_0\}$ —the sphere-dipole system comprises a nanoantenna array with two ED elements:

the nanosphere operating predominantly as an electric dipole, and the electric dipole emitter itself. In Fig. 3(c)/top, we plot the magnitudes of non-negligible expansion coefficients that contribute to  $\mathbf{E}^{\text{rad}}$  for the sphere-dipole system as a whole. The green dashed line indicates  $\lambda_0 = 681$  nm, where  $\max\{D_0\}$  and Huygens-like directivity are achieved [see Figs. 2(a) and 2(c)]. The multipolar decomposition in Fig. 3(c)/top reveals that the radiation of the array is not only due to the dipolar moments  $a_{01}$  and  $b_{\pm 1,1}$  but also due to higher-order quadrupolar moments  $a_{\pm 12}$  and  $b_{\pm 2,2}$  that are induced by the coupling between the sphere and the emitter. In Fig. 3(c)/bottom, we plot the absolute phase differences  $|a_{01} - b_{11}|$  and  $|a_{12} - b_{22}|$  between MD/ED and MQ/EQ moments, respectively. At 681 nm, the dipole moments oscillate almost in phase—phase difference  $\approx 4^\circ$ —while the quadrupole moments are in phase quadrature—phase difference  $\approx 85^\circ$ . These MD/ED moments interfere constructively toward the  $+x$ -axis direction and destructively toward the  $-x$ -axis direction, producing the Huygens-like directivity [43] depicted in Fig. 2(c). This spectral behavior is similar to the first Kerker condition of plane-wave scattering [34–36], where in-phase and equal-in-magnitude MD/ED moments result in almost zero backscattering and enhanced forward scattering.

Next, we study the radiation of a two-element  $\text{WS}_2$  sphere-dipole array consisting of a  $R = 100$  nm-radius sphere and a vertical ( $z$ -oriented) infinitesimal electric dipole. The latter is located at  $d = 200$  nm on the  $x$  axis and its dipole moment points toward the  $+z$  axis, as illustrated in the inset of Fig. 4(a). The optic axis of the  $\text{WS}_2$  sphere coincides with the  $z$  axis. In Fig. 4(a), we plot  $D_0 \equiv D(90^\circ, 0^\circ)$  and  $D_{180} \equiv D(90^\circ, 180^\circ)$  as a function of  $\lambda_0$ . The black/gray curves are computed by the semianalytical method of Sec. II using the same truncation value of  $N_c = 8$  and are in excellent agreement with the HFSS' finite-element solver (black/gray dots). Contrary to the response of Fig. 2(a), where in the vicinity of the sphere's ED resonance (i.e., at  $\lambda_0 = 679$  nm) a global  $\max\{D_0\}$  occurs, here  $D_{180}$  acquires a local maximum in the same vicinity at 684 nm. The global  $\max\{D_{180}\}$  is established at 620 nm, which is well separated from the sphere's ED resonance. The directivity values at 684 nm are  $D_{180} = 2.64$  and  $D_0 = 0.38$ , with the former being much lower than the 4.23 value observed in Fig. 2(a) for the  $\max\{D_0\}$  when the dipole is oriented horizontally. In Fig. 4(b), we plot  $D$  on the  $xy$  (left) and  $xz$  plane (right), when the sphere-dipole array operates at 684 nm. Again, the semianalytical method (blue curves) is in excellent agreement with HFSS (blue dots). Contrary to the  $+x$ -axis directed pattern of  $D$  when the dipole is horizontal [see Fig. 2(c)], the main lobe of  $D$  now points toward the  $-x$  axis. Although the value of  $D_{180}$  is non-negligible and  $D_0$  is well suppressed, this situation does not correspond to a Huygens-like directivity since lateral lobes exist, as depicted in Figs. 4(b)/left and 4(b)/right.

In Fig. 5, we perform a multipolar decomposition for the total radiated electric field  $\mathbf{E}^{\text{rad}}$  of the sphere-dipole system, when the dipole is oriented vertically. Only the contribution of non-negligible expansion coefficients is depicted. The various quantities in Fig. 5(a), which are indicated by the subscript  $N$ , are plotted normalized with respect to the maximum magnitude in the examined spectral range. The decomposition

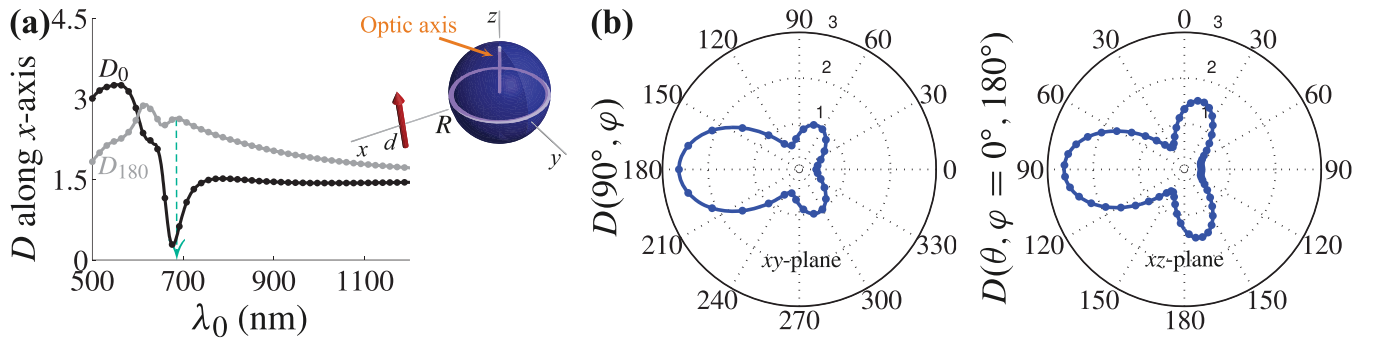


FIG. 4. (a) Directivities along the  $x$  axis of the 100-nm-radius  $\text{WS}_2$  sphere-dipole nanoarray, with the dipole oriented vertically and located at 200 nm on  $x$  axis. Black:  $D_0 \equiv D(90^\circ, 0^\circ)$  at  $+x$  axis; black curve: Semianalytical method; black dots: HFSS. Gray:  $D_{180} \equiv D(90^\circ, 180^\circ)$  at  $-x$  axis; gray curve: Semianalytical method; gray dots: HFSS. Green dashed arrowhead line:  $\lambda_0 = 684$  nm [close vicinity of ED resonance—see Fig. 2(b)]. Inset: Radiation problem of a  $\text{WS}_2$  sphere excited by a  $z$ -oriented electric dipole. The optic axis of the sphere coincides with  $z$  axis. (b) Directivities on  $xy$  and  $xz$  planes when the dipole radiates at 684 nm. Blue curves: Semianalytical method; blue dots: HFSS.

reveals that the radiation of the array is due to the dipolar moments  $a_{\pm 1,1}$  and  $b_{01}$ , as well as to the quadrupolar moments  $a_{\pm 2,2}$  and  $b_{\pm 1,2}$  that are also induced by the coupling between the sphere and the vertical dipole. In Fig. 5(b), we plot the absolute phase differences  $|\angle a_{11} - \angle b_{01}|$  and  $|\angle a_{22} - \angle b_{12}|$  between MD/ED and MQ/EQ moments, respectively. At 684 nm—i.e., at the vicinity of the sphere's ED resonance where  $D_{180}$  has its local maximum—the vertical dipole results in oscillating MD/ED and MQ/EQ moments—phase differences  $\approx 39^\circ$  and  $\approx 82^\circ$ , respectively, that present no strong interference (constructive or destructive) in any direction. In addition, this state yields a local maximum in  $D_{180}$  which is lower than the global maximum of  $D_0$  when the dipole is horizontal. To complete the analysis, we note the in-phase oscillation of MD/ED moments—phase difference  $\approx 1^\circ$ —at  $\lambda_0 = 627$  nm [shown by the sharp draugh in Fig. 5(b)]. This state, however, is of no interest because it corresponds to a negligible ED moment contribution [depicted by the sharp draugh of the  $|b_{01}|_N$  curve in Fig. 5(a)], therefore resulting in a trivial directivity pattern, not useful for the development of high end-fire directivity nanoantennas. In conclusion, a vertical dipole emitter renders the  $\text{WS}_2$  sphere-dipole array's performance poor in terms of high directivity, owing

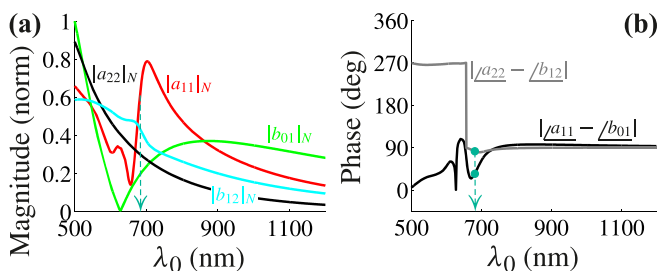


FIG. 5. (a) Normalized magnitudes of the dominant electric and magnetic expansion coefficients for the sphere-dipole nanoarray of Fig. 4(a). Red:  $|a_{11}|_N$  (MD moment); green:  $|b_{01}|_N$  (ED moment); black:  $|a_{22}|_N$  (MQ moment); cyan:  $|b_{12}|_N$  (EQ moment). Green dashed arrowhead line:  $\lambda_0 = 684$  nm [see Fig. 4(a)]. (b) Absolute phase difference between MD/ED and MQ/EQ moments. Black:  $|\angle a_{11} - \angle b_{01}|$ ; gray:  $|\angle a_{22} - \angle b_{12}|$ . Green dashed arrowhead line: Same as Fig. 5(a).

to the high AR of  $\text{WS}_2$ , in contrast to a high-index isotropic sphere-dipole array in which, due to material symmetry, the orientation of the emitter is irrelevant. Nonetheless, the high AR exhibited by  $\text{WS}_2$  has a unique impact on achieving directionality inversion, as discussed in Sec. V.

Next, we use our semianalytical method to further investigate how the properties of the sphere-dipole nanoarray depend on material anisotropy. We first notice that in the 500 nm–826.6 nm regime, i.e., the common dispersion range of  $\text{WS}_2$  and Si,  $\text{WS}_2$  has average  $\text{Re}\{\epsilon_1\}$  and  $\text{Re}\{\epsilon_3\}$  values of  $19.11\epsilon_0$  and  $6.75\epsilon_0$ , respectively, while Si an average  $\text{Re}\{\epsilon_{\text{Si}}\}$  value of  $15.08\epsilon_0$ . We therefore keep fixed the ordinary permittivity element at the high value of  $\epsilon_1 = 20\epsilon_0$  and vary the extraordinary element  $\epsilon_3$  so the material from isotropic ( $\epsilon_3 = 20\epsilon_0$ ) becomes NU ( $\epsilon_1 > \epsilon_3$  with  $\epsilon_3 = 15\epsilon_0, 10\epsilon_0, 5\epsilon_0$ ). In all cases,  $\mu_s = \mu_0$ . Defining the AR as  $\text{AR} = |(\epsilon_1 - \epsilon_3)/(\epsilon_1 + \epsilon_3)|$ , the extreme values of  $(\epsilon_1, \epsilon_3) = (20\epsilon_0, 5\epsilon_0)$  yield  $\text{AR} = 0.6$ , while  $\text{AR} = 0$  for the isotropic case. In Fig. 6(a), we examine a 100-nm-radius sphere-dipole nanoarray, with the dipole oriented horizontally on the  $x$  axis for three different values of  $d = 150, 200, 250$  nm. In particular, we plot the specific values of  $\max\{D_0\}$  for different values of AR, when Huygens-like directivity takes place. That is to say, for each depicted value of  $\max\{D_0\}$  in Fig. 6(a), the MD/ED moments oscillate almost in phase, interfere constructively toward the  $+x$ -axis direction and destructively toward the  $-x$ -axis direction, and ultimately produce radiation patterns similar to the ones depicted in Fig. 2(c). From the results of Fig. 6(a) we observe that, as AR acquires higher values, the  $\lambda_0$  for which the MD/ED moments oscillate in phase undergoes a blueshift. For instance, for the  $d = 250$  nm case, if we define the  $\lambda_0 = 699$  nm/isotropic material (black circle) as the reference point, a NU increment in the AR such as  $\text{AR} = 0.14$  (black square),  $\text{AR} = 0.33$  (black diamond), and  $\text{AR} = 0.6$  (black star), blueshifts  $\lambda_0$  at 694 nm, 690 nm, and 687 nm, respectively. This behavior is also observed for the other two examples with  $d = 150$  and 200 nm. Although the discussion in Fig. 6(a) concerns a horizontally oriented dipole, we have also performed the same study for a vertically oriented dipole. In this case, however, except for the isotropic state where (due to material symmetry) the orientation of the dipole does not affect the response of the system, there are no points of notable

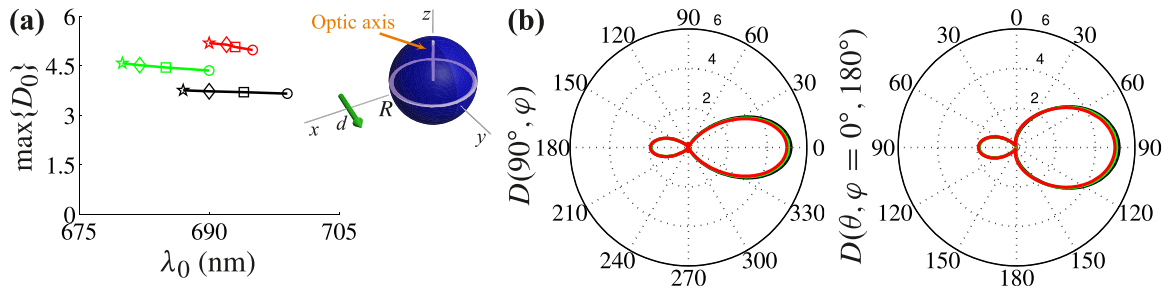


FIG. 6. (a) Values of  $\max\{D_0\}$  at  $\lambda_0$  for which Huygens-like directivity takes place, for various values of AR. The configuration consists of an 100 nm-radius sphere-dipole nanoarray, with the dipole oriented horizontally on  $x$  axis. Red curve:  $d = 150$  nm; green curve:  $d = 200$  nm; black curve:  $d = 250$  nm. In all cases  $\epsilon_1 = 20\epsilon_0$ . Circles:  $\epsilon_3 = 20\epsilon_0$ ; squares:  $\epsilon_3 = 15\epsilon_0$ ; diamonds:  $\epsilon_3 = 10\epsilon_0$ ; stars:  $\epsilon_3 = 5\epsilon_0$ . In all cases,  $\mu_s = \mu_0$ . (b) Directivities in  $xy$  and  $xz$  planes for  $d = 150$  nm. Red curves:  $\lambda_0 = 695$  nm for which  $\max\{D_0\} = 4.98$  [red circle in Fig. 6(a)]; green curves:  $\lambda_0 = 693$  nm for which  $\max\{D_0\} = 5.07$  [red square in Fig. 6(a)]; black curves:  $\lambda_0 = 690$  nm for which  $\max\{D_0\} = 5.19$  [red star in Fig. 6(a)].

interest where the MD/ED moments oscillate in phase and could result in strong interference (constructive or destructive) in a specific direction. Consequently, for a NU sphere, a vertical dipole does not lead to an asymmetric Huygens-like radiation pattern in directivity. In Fig. 6(b), we plot  $D$  on  $xy$  and  $xz$  planes for the  $d = 150$  nm case of Fig. 6(a) and for the three different values of AR, i.e., AR = 0 (red circle), AR = 0.14 (red square), and AR = 0.6 (red star). As evident, all three states maintain an asymmetric radiation pattern in  $D$ ; specifically,  $\max\{D_0\}$  increases progressively from 4.98 (AR = 0) to 5.07 (AR = 0.14) and 5.19 (AR = 0.6). The intermediate state with AR = 0.33 (red diamond), yields  $\max\{D_0\} = 5.14$  at  $\lambda_0 = 692$  nm and has a pattern similar to the ones depicted in Fig. 6(b); these curves, however, are not depicted to present a clear figure and avoid a dense image. In conclusion, anisotropy renders the operation of the two-element sphere-dipole array dependent on the relative orientation of the dipole emitter, and blueshifts the desired  $\lambda_0$  with respect to the isotropic state.

To complete the investigation of sphere-dipole nanoarrays, we discuss how the asymmetric Huygens-like directivity depends on fine-tuning of the distance  $d$  of the dipole emitter, as well as on  $\lambda_0$ . To this end, we employ our semianalytical method and examine two cases of  $\text{WS}_2$  spheres having radii 100 nm and 150 nm, respectively. In both scenarios, we vary  $d$  in steps of 10 nm and examine how the  $\max\{D_0\}$  and the front-to-back ratio (FBR) are affected with respect

to this parameter. We point out that each depicted value of  $\max\{D_0\}$  and FBR in Fig. 7(a) corresponds to an almost in-phase oscillation of MD/ED moments. We observe that, as  $d$  changes, global maxima in  $\max\{D_0\}$  and FBR appear, for different values of  $d$ . These optimal states, as depicted by the green arrowhead lines in Fig. 7(a), occur at different  $\lambda_0$ . For instance, the peak of  $\max\{D_0\} = 5.0$  for the 100-nm-radius sphere occurs at  $d = 140$  nm for  $\lambda_0 = 688$  nm, while the peak of FBR = 3.79 at  $d = 160$  nm for  $\lambda_0 = 683$  nm; at this latter wavelength,  $\max\{D_0\} = 4.81$ . For the 150-nm-radius sphere, the peak of  $\max\{D_0\} = 4.82$  occurs at  $d = 220$  nm for  $\lambda_0 = 945$  nm, while the peak of FBR = 3.11 at  $d = 250$  nm for  $\lambda_0 = 938$  nm; at this latter wavelength,  $\max\{D_0\} = 4.64$ . In Fig. 7(b), we plot  $D$  on  $xy$  and  $xz$  planes for the 100-nm-radius example of Fig. 7(a) and three different values of  $d$ . As evident, all states maintain an asymmetric radiation pattern in  $D$ , thus proving the robustness of the results to the change of  $d$ .

Finally, in Fig. 8 we show that the principle discussed for the two-element TMDC sphere-dipole array can be applied for a TMDC disk-dipole array. In Fig. 8(a), we plot  $D_0$  and  $D_{180}$  versus  $\lambda_0$  for a 100-nm-radius and 95-nm-high  $\text{WS}_2$  disk-dipole array, when the dipole is oriented horizontally. The  $\max\{D_0\} = 4.25$  is observed at 679 nm, i.e., at the close vicinity of the disk's ED resonance [19]. The latter is located at 675 nm, as depicted in Fig. 8(b) where we plot the total scattering cross section  $Q_{sc}$  due to a TE plane wave— $\mathbf{E}^{\text{inc}}$  is

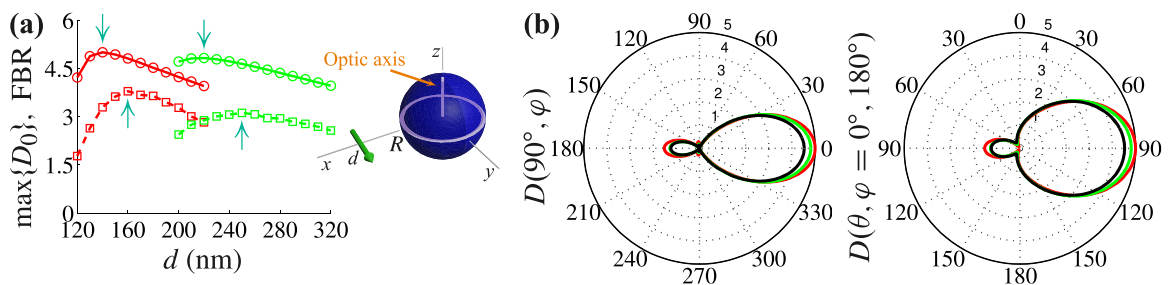


FIG. 7. (a) Values of  $\max\{D_0\}$  and FBR versus  $d$  for which Huygens-like directivity takes place. The configuration consists of a  $\text{WS}_2$  sphere-dipole nanoarray, with the dipole oriented horizontally on  $x$  axis. Red curves:  $R = 100$  nm; green curves:  $R = 150$  nm. Circles:  $\max\{D_0\}$ ; squares: FBR. Green arrowhead lines: Optimal states at which  $\max\{D_0\}$  and FBR are maximized. (b) Directivities in  $xy$  and  $xz$  planes when  $R = 100$  nm. Red curves:  $d = 140$  nm and  $\lambda_0 = 688$  nm for which the peak  $\max\{D_0\} = 5.0$  is observed; green curves:  $d = 160$  nm and  $\lambda_0 = 683$  nm for which the peak FBR = 3.79 is observed; black curves:  $d = 180$  nm and  $\lambda_0 = 681$  nm.



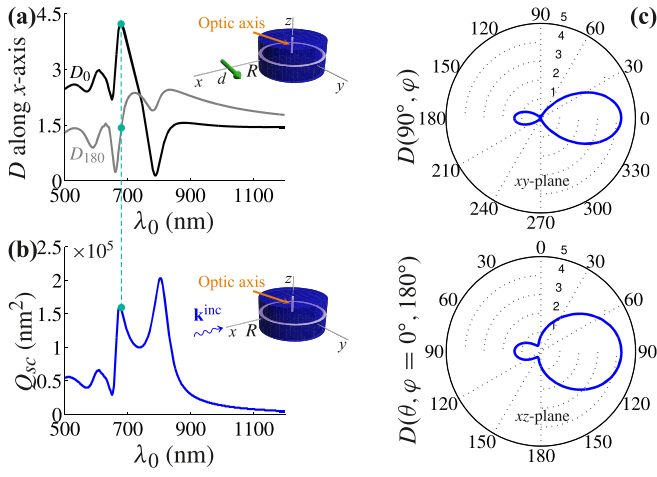


FIG. 8. (a) Directivities along the  $x$  axis of the 100-nm-radius and 95-nm-high  $\text{WS}_2$  disk-dipole array, with the dipole located at 200 nm on  $x$  axis. Black:  $D_0 \equiv D(90^\circ, 0^\circ)$  at  $+x$  axis (via HFSS). Gray:  $D_{180} \equiv D(90^\circ, 180^\circ)$  at  $-x$  axis (via HFSS). Green dashed arrowhead line:  $\lambda_0 = 679$  nm [close vicinity of ED resonance—see Fig. 8(b)]. Inset: Radiation problem of a  $\text{WS}_2$  disk excited by a  $y$ -oriented electric dipole. The optic axis of the disk coincides with  $z$  axis. (b) Plane-wave scattering spectrum of a 100-nm-radius and 95-nm-high  $\text{WS}_2$  disk illuminated by a TE-polarized plane wave impinging from the  $+x$  axis. Blue: Total  $Q_{sc}$  (via HFSS). Green dashed line: Projection of 679 nm (the ED resonance is located at 675 nm and the MD resonance at 804 nm). Inset: Plane-wave scattering from a  $\text{WS}_2$  disk. (c) Directivities on  $xy$  and  $xz$  planes, when the dipole radiates at 679 nm (via HFSS).

$y$  polarized and  $\mathbf{k}^{\text{inc}}$  is directed along the  $+x$  axis—scattered from the  $\text{WS}_2$  disk. In Fig. 8(c), we plot  $D$  on  $xy$  (top) and  $xz$  planes (bottom) when the dipole radiates at 679 nm. The patterns of  $D$  are Huygens-like, similar to the patterns of the  $\text{WS}_2$  sphere-dipole array analyzed in Fig. 2(c). On the other hand, a vertical emitter renders the performance of the  $\text{WS}_2$  disk-dipole array poor in terms of high directivity, in a manner similar to the one discussed above.

#### IV. HIGH END-FIRE DIRECTIVITY TMDC NANOANTENNA

We apply the principles presented for the two-element  $\text{WS}_2$  sphere-dipole array to demonstrate that larger arrays of  $\text{WS}_2$  elements may be used to build a high end-fire directivity nanoantenna, useful in potential applications in the context of all-anisotropic nanophotonics. To complement our study of spherical  $\text{WS}_2$  elements, we also demonstrate the feasibility of such a realization using cylindrical disk  $\text{WS}_2$  elements. First, we consider a  $\text{WS}_2$  spherical nanoantenna array consisting of four 100-nm-radius directors and one 110-nm-radius reflector, as depicted in the inset of Fig. 9(a). The gaps between the directors, between the first director and the dipole, and between the reflector and the dipole, are the same and equal to 100 nm. Such reflector-director configurations are known as Yagi-Uda nanoantennas [9], the term originating from the Yagi-Uda antenna used for television reception [41]. To make an initial estimation of the  $\lambda_0$  at which the spherical nanoantenna array yields its global  $\max\{D_{\text{max}}\}$ , with  $D_{\text{max}} \equiv$

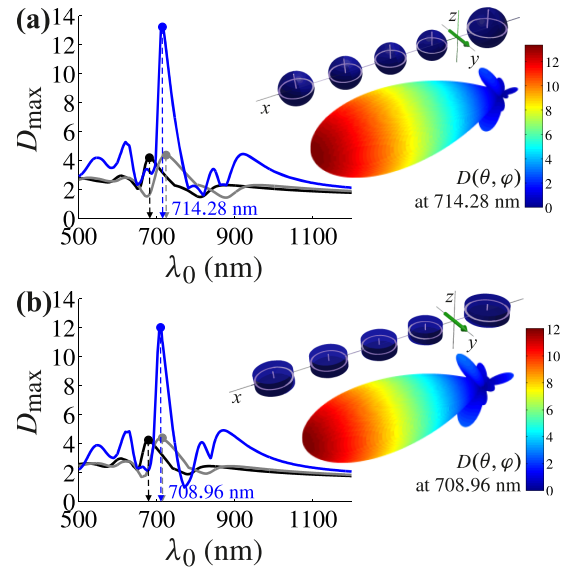


FIG. 9. Designing a high end-fire directivity  $\text{WS}_2$  nanoantenna array. (a) Maximum directivity versus wavelength, using spherical elements. Black: 100-nm-radius sphere-dipole array (semianalytical method)/black dashed arrowhead line:  $\lambda_0 = 681$  nm; gray: 110-nm-radius sphere-dipole array (semianalytical method)/gray dashed arrowhead line:  $\lambda_0 = 723$  nm; blue: nanoantenna array (HFSS)/blue dashed arrowhead line:  $\lambda_0 = 714.28$  nm. Inset:  $\text{WS}_2$  spherical nanoantenna array consisting of four directors and one reflector, and 3D polar pattern of  $D(\theta, \varphi)$  at 714.28 nm. The radii of all directors are equal to 100 nm, the radius of the reflector is 110 nm, and the gaps between the directors, between the first director and the dipole, and between the reflector and the dipole, are the same and equal to 100 nm. (b) Maximum directivity versus wavelength, using cylindrical disk elements (via HFSS). Legends are the same as in Fig. 9(a) except the  $\lambda_0$  at various  $\max\{D_{\text{max}}\}$ . Black dashed arrowhead line:  $\lambda_0 = 679$  nm; gray dashed arrowhead line:  $\lambda_0 = 710$  nm; blue dashed arrowhead line:  $\lambda_0 = 708.96$  nm. Inset:  $\text{WS}_2$  cylindrical disk nanoantenna array consisting of four directors and one reflector, and 3D polar pattern of  $D(\theta, \varphi)$  at 708.96 nm. The heights of all elements are equal to 95 nm, the radii of all directors are equal to 100 nm, the radius of the reflector is 110 nm, and the gaps between the directors, between the first director and the dipole, and between the reflector and the dipole, are the same and equal to 100 nm.

$\max\{D(\theta, \varphi)\}$ , we apply the principles presented above for the two-element  $\text{WS}_2$  sphere-dipole array and plot in Fig. 9(a) the  $D_{\text{max}}$  versus  $\lambda_0$  for the 100-nm-radius sphere-dipole array (black curve) and for the 110-nm-radius sphere-dipole array (gray curve), using our semianalytical method. The global  $\max\{D_{\text{max}}\}$  for the 100-nm- and 110-nm-radius sphere-dipole arrays are observed at 681 nm and 723 nm, respectively. The  $\lambda_0$  for which the spherical nanoantenna array yields its  $\max\{D_{\text{max}}\}$  is therefore anticipated in the neighborhood of 681 nm and 723 nm. Using HFSS, we calculate  $D_{\text{max}}$  for the spherical nanoantenna array in the 500 nm–1200 nm regime, as depicted by the blue curve in Fig. 9(a), and conclude that the global  $\max\{D_{\text{max}}\}$  is observed at  $\lambda_0 = 714.28$  nm. At this wavelength, the three-dimensional (3D) polar pattern of  $D(\theta, \varphi)$ —inset of Fig. 9(a)—is highly directive with  $\max\{D_{\text{max}}\} = 13.35$  and a FBR of 10.67, while its main lobe points toward the  $+x$  axis. We found that the wavelength

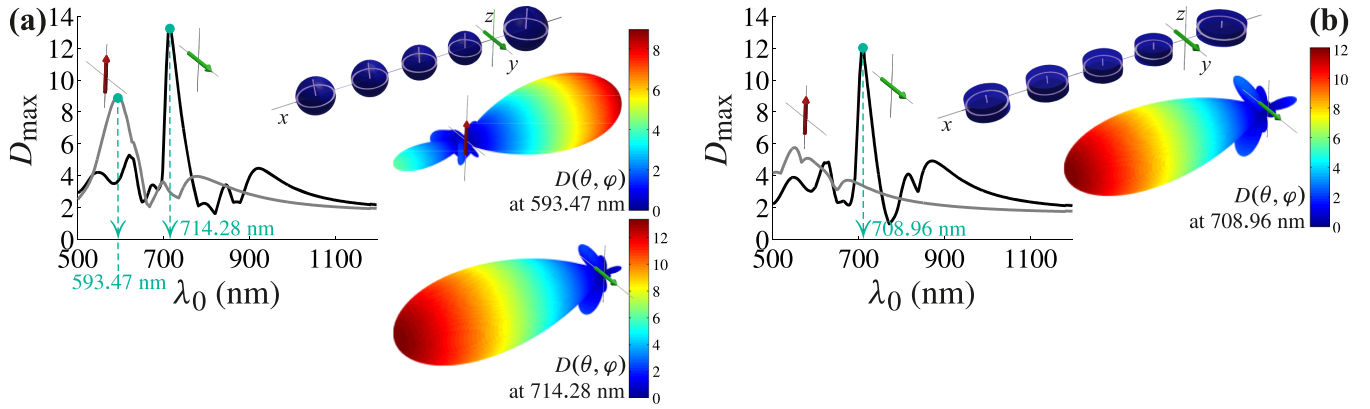


FIG. 10. (a) Maximum directivity versus wavelength, using spherical elements. Black:  $y$ -oriented dipole (via HFSS); gray:  $z$ -oriented dipole (via HFSS). Left green dashed arrowhead line:  $\lambda_0 = 593.47$  nm (vertical dipole); right green dashed arrowhead line:  $\lambda_0 = 714.28$  nm (horizontal dipole). Top inset:  $\text{WS}_2$  spherical nanoantenna array consisting of four directors and one reflector. The radii of all directors are equal to 100 nm, the radius of the reflector is 110 nm, and the gaps between the directors, between the first director and the dipole, and between the reflector and the dipole, are the same and equal to 100 nm [same setup parameters as in Fig. 9(a)]. Middle inset: 3D polar pattern of  $D(\theta, \varphi)$  at 593.47 nm. Bottom inset: 3D polar pattern of  $D(\theta, \varphi)$  at 714.28 nm. (b) Maximum directivity versus wavelength, using cylindrical disk elements. Black:  $y$ -oriented dipole (via HFSS); gray:  $z$ -oriented dipole (via HFSS). Green dashed arrowhead line:  $\lambda_0 = 708.96$  nm. Top inset:  $\text{WS}_2$  cylindrical disk nanoantenna array consisting of four directors and one reflector. The heights of all elements are equal to 95 nm, the radii of all directors are equal to 100 nm, the radius of the reflector is 110 nm, and the gaps between the directors, between the first director and the dipole, and between the reflector and the dipole, are the same and equal to 100 nm [same setup parameters as in Fig. 9(b)]. Bottom inset: 3D polar pattern of  $D(\theta, \varphi)$  at 708.96 nm.

giving the above-mentioned global maximum can be tuned by appropriately engineering the gap and the size of the reflector/directors.

In Fig. 9(b), we demonstrate the feasibility of a high end-fire directivity cylindrical nanoantenna array, by employing  $\text{WS}_2$  disk elements. Such nanodisks were recently fabricated by combined electron-beam lithography and dry etching at various heights, ranging from 55 nm up to 150 nm, and at various radii ranging from 95 nm up to 200 nm [19]. The cylindrical disk nanoantenna array is illustrated in the inset of Fig. 9(b) and consists of four 100-nm-radius directors and one 110-nm-radius reflector, while the heights of all elements are equal to 95 nm. The gaps between the directors, between the first director and the dipole, and between the reflector and the dipole, are the same and equal to 100 nm. From the solution of the disk-dipole array problem, we can estimate the  $\lambda_0$  at which the cylindrical disk nanoantenna array yields its global  $\max\{D_{\max}\}$ . In particular, the black and gray curves in Fig. 9(b) depict the  $D_{\max}$  versus  $\lambda_0$ —via HFSS—for the 100-nm- and 110-nm-radius disk-dipole arrays, respectively. The global  $\max\{D_{\max}\}$  corresponding to the two setups are located at 679 nm and 710 nm, respectively. The global  $\max\{D_{\max}\} = 12.05$  for the cylindrical disk nanoantenna array (blue curve) occurs at 708.96 nm, thus confirming the applicability of the principles discussed above. The inset of Fig. 9(b) depicts the highly directive 3D polar pattern of  $D(\theta, \varphi)$ , having a 6.34 FBR value.

Finally, we study the performance of the  $\text{WS}_2$  spherical/cylindrical nanoantenna arrays introduced in Fig. 9, in terms of high end-fire directivity, when the dipole emitter is vertically oriented, and compare it with the respective performance obtained for a horizontally oriented dipole. This comparison is presented in Fig. 10(a) for the case of the spherical nanoantenna array, and in Fig. 10(b)

for the cylindrical counterpart, via HFSS. The parameter values for the two nanoantenna setups are the same as the ones employed in Fig. 9. From Figs. 10(a) and 10(b), we conclude that if the nanoantenna arrays are stimulated by a vertical dipole, the maximum values of  $D_{\max}$  are lower than the global maxima of  $D_{\max}$  when the arrays are stimulated by a horizontal dipole. For instance,  $\max\{D_{\max}\} = 8.96$  at  $\lambda_0 = 593.47$  nm for the case of the vertical dipole [gray curve in Fig. 10(a)] is significantly lower than  $\max\{D_{\max}\} = 13.35$  at  $\lambda_0 = 714.28$  nm for the case of the horizontal dipole [black curve in Fig. 10(a)]. In addition, the wavelength  $\lambda_0 = 593.47$  nm is not close to the two ED resonances of the director/reflector spheres (the ED resonances of the 100-nm-radius director and 110-nm-radius reflector are at 679 nm and 712 nm, respectively), which further implies that  $D(\theta, \varphi)$  is not as directive, with a FBR = 2.16, as clearly illustrated in the middle inset of Fig. 10(a). We also note that in this case, the main lobe points toward the  $-x$  axis. For comparison, in the bottom inset of Fig. 10(a), we also depict the 3D polar pattern of  $D(\theta, \varphi)$  when the spherical nanoantenna array is excited at  $\lambda_0 = 714.28$  nm by a horizontal dipole, with FBR = 10.67 and the main lobe pointing toward the  $+x$  axis [the respective plot for the cylindrical nanoantenna array is given in the inset of Fig. 10(b)]. We therefore deduce that the proposed anisotropic  $\text{WS}_2$  configurations exhibit high end-fire directivities when the dipole is horizontally oriented, while a poor performance is obtained for the vertical orientation, owing to the high AR of  $\text{WS}_2$ .

## V. DIRECTIONALITY INVERSION

We now show that TMDC anisotropy may be employed to achieve directionality inversion in the directivity of a

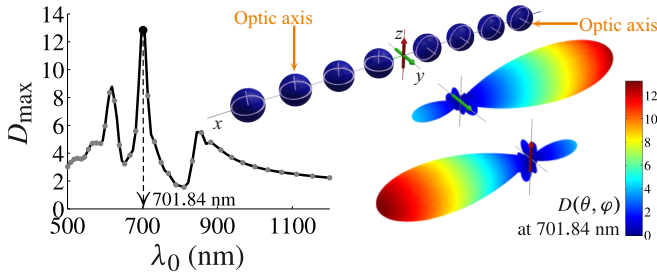


FIG. 11. Maximum directivity versus operating wavelength (via HFSS) for a WS<sub>2</sub> nanoantenna array featuring high end-fire directionality inversion. Black: Horizontal dipole; gray dots: vertical dipole; black dashed arrowhead line:  $\lambda_0 = 701.84$  nm. Inset: WS<sub>2</sub> spherical nanoantenna array and 3D polar pattern of  $D(\theta, \varphi)$  at 701.84 nm. The radii of all nanospheres are equal to 100 nm, the gaps between the particles are equal to 100 nm, and the gap between the dipole and each adjacent sphere is 100 nm. The four elements along the  $+x$  axis have a  $z$ -oriented optic axis, while the four elements along the  $-x$  axis feature a  $y$ -oriented optic axis.

nanoantenna array at the same operating  $\lambda_0$  due to orientation-based coupling between a free-to-rotate dipole emitter and the fixed WS<sub>2</sub> elements. In particular, we design a nanoantenna array consisting of spherical WS<sub>2</sub> elements, as shown in the inset of Fig. 11. The radii of all nanospheres are equal to 100 nm, the gap between each of them is 100 nm, and the gap between the dipole and each adjacent sphere is 100 nm, while the dipole emitter is free to rotate on the  $yz$  plane. Here, taking advantage of the anisotropic properties of WS<sub>2</sub>, we design the array so the elements along the  $+x$  axis have a  $z$ -oriented optic axis, while the elements along the  $-x$  axis feature a  $y$ -oriented optic axis, as illustrated in the inset of Fig. 11. In a  $\theta_0$ -angle rotated coordinate system about the  $x$  axis, the permittivity tensor  $\hat{\epsilon}(\lambda_0)$ , which has the same expression as  $\bar{\epsilon}(\lambda_0)$ , can be expressed in the global coordinate system  $Oxyz$  by the similarity transformation

$$\hat{\epsilon}(\lambda_0) = \mathbf{R}_x^{-1}(\theta_0)\bar{\epsilon}(\lambda_0)\mathbf{R}_x(\theta_0), \quad (29)$$

where  $\mathbf{R}_x(\theta_0) = (R_{ij})$ ,  $i, j = 1, 2, 3$ , is a rotation matrix with  $R_{11} = 1$ ,  $R_{22} = R_{33} = \cos \theta_0$ ,  $R_{23} = -\sin \theta_0$ ,  $R_{32} = -R_{23}$ , and  $R_{12} = R_{13} = R_{21} = R_{31} = 0$ . Employing  $\theta_0 = 90^\circ$ , Eq. (29) yields  $\hat{\epsilon}(\lambda_0) = \epsilon_1(\lambda_0)(\mathbf{e}_x\mathbf{e}_x^T + \mathbf{e}_z\mathbf{e}_z^T) + \epsilon_3(\lambda_0)\mathbf{e}_y\mathbf{e}_y^T$ . In Fig. 11, we plot  $D_{\max}$  for a horizontally oriented dipole—i.e., the dipole moment points toward the  $+y$  axis. In this case, the global  $\max\{D_{\max}\} = 13.60$  occurs at 701.84 nm. The 3D pattern of  $D(\theta, \varphi)$  is depicted in the inset of Fig. 11, revealing high directivity values toward the  $-x$  axis. This means that the spherical elements along the  $+x$  axis contribute high directivity values in the opposite direction, a behavior in accordance with the conclusions drawn for the two-element WS<sub>2</sub> sphere-dipole array in Figs. 2(a) and 2(c), where the main lobe of the directivity points to the nanoantenna's side where the dipole is located. Here, in addition, the spherical elements along the  $-x$  axis do not contribute a high directivity toward the  $+x$  axis, because their  $\mathbf{e}_y\mathbf{e}_y^T$  permittivity element is significantly smaller in the whole visible-near IR regime than that of the  $\mathbf{e}_x\mathbf{e}_x^T$ ,  $\mathbf{e}_z\mathbf{e}_z^T$  elements, due to the different orientation of those particles.

This behavior is in agreement with the conclusions of Sec. III. When the dipole is oriented vertically, with its moment pointing toward the  $+z$  axis, the role between the unrotated/rotated elements is swapped. This results in the same  $D_{\max}$  versus  $\lambda_0$  (depicted by the gray dots in Fig. 11) as with the horizontal dipole. Now, however, inversion of the  $D(\theta, \varphi)$  pattern takes place for all  $\lambda_0$ . Notably at 701.84 nm, i.e., at the same  $\lambda_0$  where  $\max\{D_{\max}\}$  for the horizontal dipole is observed, the 3D pattern of  $D(\theta, \varphi)$  has the same high value of  $\max\{D_{\max}\} = 13.60$  but now toward the  $+x$  axis. Consequently, by controlling the orientation of the dipole emitter, we can achieve high end-fire directionality inversion, as illustrated in the inset of Fig. 11. Asymmetric mode propagation and radiation has also been reported in Ref. [37] for chains of magnetodielectric particles, when the chain is externally excited by mutually orthogonal electric and magnetic dipoles. In the present case, this operation is achieved using external excitation by only one dipole. This unique feature is characteristic of the high AR exhibited by WS<sub>2</sub> in the optical-near IR regime and cannot be readily realized in isotropic all-dielectric or plasmonic spherical structures, due to their material symmetry. Thus, our material-anisotropy-based design offers an extra degree of freedom for the control of radiating nanostructures and enriches the existing nanophotonics platforms by allowing for functionalities such as directionality inversion, as well as for the implementation of high end-fire directivity nanoantennas.

## VI. CONCLUSIONS

Using a rigorous semianalytical solution for the radiation problem of an anisotropic spherical particle excited by an electric dipole and complementing this solution by full-wave finite-element simulations, we introduced a class of all-anisotropic WS<sub>2</sub> TMDC nanoantennas which exhibit high end-fire directivity and directionality inversion. Our guiding principle was the two-element WS<sub>2</sub> sphere-dipole array, which was shown to exhibit Huygens-like directivity for an excitation wavelength quite close to the particle's ED resonance. We also established that the same principle applies to nonspherical particles, such as the recently fabricated cylindrical WS<sub>2</sub> disks. Based on this principle, we further demonstrated that chain structures of spherical or cylindrical disk WS<sub>2</sub> elements may serve as high end-fire directivity nanoantenna arrays. Furthermore, we showed that, by an appropriate rotation of half the elements of the nanoantenna array, end-fire directionality inversion can be achieved at a fixed operating wavelength simply by adjusting the dipole's orientation; this unique feature is due to the high AR exhibited by WS<sub>2</sub> in the optical-near IR regime. Our findings enrich existing nanophotonics platforms and could pave the way toward the design of functional and tunable devices at the nanoscale.

## ACKNOWLEDGMENTS

This research is cofinanced by Greece and the European Union (European Social Fund-ESF) through the operational program ‘‘Human Resources Development, Education and Lifelong Learning 2014-2020’’ in the context of the project ‘‘Deep Brain Stimulation Modeling through Accurate Electrodynamical Techniques’’ (MIS No. 5047942).

- [1] D. G. Baranov, M. Wersäll, J. Cuadra, T. J. Antosiewicz, and T. Shegai, *ACS Photonics* **5**, 24 (2018).
- [2] A. Krasnok, S. Glybovski, M. Petrov, S. Makarov, R. Savelev, P. Belov, C. Simovski, and Y. Kivshar, *Appl. Phys. Lett.* **108**, 211105 (2016).
- [3] T. Feng, Y. Xu, Z. Liang, and W. Zhang, *Opt. Lett.* **41**, 5011 (2016).
- [4] V. Pacheco-Peña and M. Navarro-Cía, *Nanoscale* **10**, 13607 (2018).
- [5] H. Sugimoto and M. Fujii, *ACS Photonics* **8**, 1794 (2021).
- [6] D. G. Baranov, R. Verre, P. Karpinski, and M. Käll, *ACS Photonics* **5**, 2730 (2018).
- [7] J. Li, A. Salandrino, and N. Engheta, *Phys. Rev. B* **76**, 245403 (2007).
- [8] I. S. Maksymov, I. Staude, A. E. Miroshnichenko, and Y. S. Kivshar, *Nanophotonics* **1**, 65 (2012).
- [9] A. E. Krasnok, A. E. Miroshnichenko, P. A. Belov, and Y. S. Kivshar, *Opt. Express* **20**, 20599 (2012).
- [10] A. E. Krasnok, C. R. Simovski, P. A. Belov, and Y. S. Kivshar, *Nanoscale* **6**, 7354 (2014).
- [11] T. Shibanuma, P. Albella, and S. A. Maier, *Nanoscale* **8**, 14184 (2016).
- [12] K. R. Mahmoud, M. Hussein, M. F. O. Hameed, and S. S. A. Obayya, *J. Opt. Soc. Am. B* **34**, 2041 (2017).
- [13] R. S. Savelev, O. N. Sergaeva, D. G. Baranov, A. E. Krasnok, and A. Alú, *Phys. Rev. B* **95**, 235409 (2017).
- [14] J. Li, A. Salandrino, and N. Engheta, *Phys. Rev. B* **79**, 195104 (2009).
- [15] S. J. Norton and T. Vo-Dinh, *IEEE Trans. Nanotechnol.* **11**, 1264 (2011).
- [16] Y. Sun, V. Yaroshenko, A. Chebykin, E. Ageev, S. Makarov, and D. Zuev, *Opt. Mat. Expr.* **10**, 29 (2020).
- [17] Z. E. Stamatopoulou and C. Tserkezis, *OSA Continuum* **4**, 918 (2021).
- [18] M. K. Schmidt, R. Esteban, J. J. Sáenz, I. Suárez-Lacalle, S. Mackowski, and J. Aizpurua, *Opt. Express* **20**, 13636 (2012).
- [19] R. Verre, D. G. Baranov, B. Munkhbat, J. Cuadra, M. Käll, and T. Shegai, *Nat. Nanotechnol.* **14**, 679 (2019).
- [20] T. D. Green, D. G. Baranov, B. Munkhbat, R. Verre, T. Shegai, and M. Käll, *Optica* **7**, 680 (2020).
- [21] G. A. Ermolaev, D. V. Grudinin, Y. V. Stebunov, K. V. Voronin, V. G. Kravets, J. Duan, A. B. Mazitov, G. I. Tselikov, A. Bylinkin, D. I. Yakubovsky, S. M. Novikov, D. G. Baranov, A. Y. Nikitin, I. A. Kruglov, T. Shegai, P. Alonso-González, A. N. Grigorenko, A. V. Arsenin, K. S. Novoselov, and V. S. Volkov, *Nat. Commun.* **12**, 854 (2021).
- [22] F. Hu, Y. Luan, M. E. Scott, J. Yan, D. G. Mandrus, X. Xu, and Z. Fei, *Nature Photon.* **11**, 356 (2017).
- [23] F. Hu and Z. Fei, *Adv. Optical Mater.* **8**, 1901003 (2019).
- [24] D. Hu, K. Chen, X. Chen, X. Guo, M. Liu, and Q. Dai, *Adv. Mater.* **31**, 1807788 (2019).
- [25] R. Mupparapu, T. Bucher, and I. Staude, *Adv. Phys. X* **5**, 1734083 (2020).
- [26] C. Schmidt and U. van Rienen, *IEEE Trans. Biomed. Eng.* **59**, 1583 (2012).
- [27] D. P. Chrissoulidis and J.-M. Laheurte, *IEEE Trans. Antennas Propag.* **64**, 4984 (2016).
- [28] R. W. Ziolkowski and A. D. Kipple, *IEEE Trans. Antennas Propag.* **51**, 2626 (2003).
- [29] X. Zambrana-Puyalto and N. Bonod, *Phys. Rev. B* **91**, 195422 (2015).
- [30] H. Chew, *J. Chem. Phys.* **87**, 1355 (1987).
- [31] P. Prokopiou and N. L. Tsitsas, *Studies Appl. Math.* **140**, 438 (2018).
- [32] L.-W. Li, P.-S. Kooi, M.-S. Leong, and T.-S. Yeo, *IEEE Trans. Microw. Theory Techn.* **42**, 2302 (1994).
- [33] C.-T. Tai, *Dyadic Green's Functions in Electromagnetic Theory* (IEEE, New York, 1994).
- [34] J. M. Geffrin, B. García-Cámara, R. Gómez-Medina, P. Albella, L. S. Froufe-Pérez, C. Eyraud, A. Litman, R. Vaillon, F. González, M. Nieto-Vesperinas, J. J. Sáenz, and F. Moreno, *Nat. Commun.* **3**, 1171 (2012).
- [35] G. D. Kolezas, G. P. Zouros, and K. L. Tsakmakidis, *IEEE J. Sel. Top. Quantum Electron.* **25**, 4700912 (2019).
- [36] G. D. Kolezas, G. P. Zouros, G. K. Pagiatakis, and J. A. Roumeliotis, *IEEE J. Sel. Top. Quantum Electron.* **27**, 8300312 (2021).
- [37] Y. Mazor and B. Z. Steinberg, *Phys. Rev. B* **94**, 235114 (2016).
- [38] J. L.-W. Li and W.-L. Ong, *IEEE Trans. Antennas Propag.* **59**, 3370 (2011).
- [39] W. C. Chew, *Waves and Fields in Inhomogeneous Media* (Van Nostrand Reinhold, New York, 1990).
- [40] P. M. Morse and H. Feshbach, *Methods of Theoretical Physics* (McGraw-Hill, New York, 1953).
- [41] C. A. Balanis, *Antenna Theory: Analysis and Design* (John Wiley & Sons, Inc., New York, 1982).
- [42] D. E. Aspnes and A. A. Studna, *Phys. Rev. B* **27**, 985 (1983).
- [43] S. D. Campbell and R. W. Ziolkowski, *IEEE J. Sel. Topics Quantum Electron.* **19**, 4700209 (2013).